

## Ionization front in a high-current gas discharge(a)

Edgar Y. Choueiri and Thomas M. Randolph

Citation: *Physics of Plasmas* **14**, 033502 (2007); doi: 10.1063/1.2646365

View online: <http://dx.doi.org/10.1063/1.2646365>

View Table of Contents: <http://scitation.aip.org/content/aip/journal/pop/14/3?ver=pdfcov>

Published by the [AIP Publishing](#)

---

### Articles you may be interested in

[Mass dependency of turbulent parameters in stationary glow discharge plasmas](#)

*Phys. Plasmas* **20**, 052304 (2013); 10.1063/1.4804339

[Three-dimensional particle-in-cell simulation of discharge characteristics in cylindrical anode layer hall plasma accelerator](#)

*Phys. Plasmas* **19**, 043507 (2012); 10.1063/1.3703321

[Spatially resolved high-resolution x-ray spectroscopy of high-current plasma-focus discharges\(a\)](#)

*Rev. Sci. Instrum.* **81**, 10E312 (2010); 10.1063/1.3483190

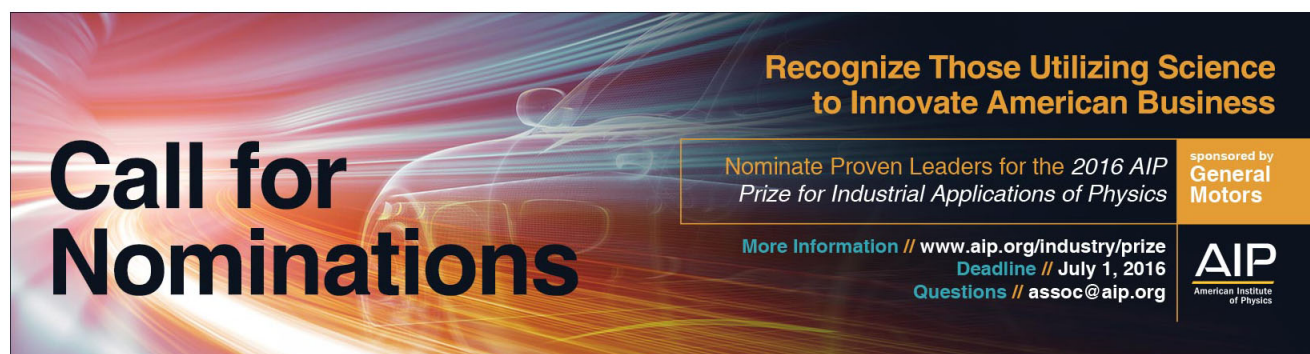
[Production of highly ionized species in high-current pulsed cathodic arcs](#)

*Appl. Phys. Lett.* **96**, 221501 (2010); 10.1063/1.3442509

[Tomographic interferometry of a filtered high-current vacuum arc plasma](#)

*J. Appl. Phys.* **101**, 073302 (2007); 10.1063/1.2714677

---



**Call for Nominations**

**Recognize Those Utilizing Science to Innovate American Business**

Nominate Proven Leaders for the *2016 AIP Prize for Industrial Applications of Physics*

More Information // [www.aip.org/industry/prize](http://www.aip.org/industry/prize)  
Deadline // July 1, 2016  
Questions // [assoc@aip.org](mailto:assoc@aip.org)

sponsored by  
**General Motors**

**AIP**  
American Institute of Physics

# Ionization front in a high-current gas discharge<sup>a)</sup>

Edgar Y. Choueiri

*Electric Propulsion and Plasma Dynamics Laboratory, Princeton University, Princeton, New Jersey 08544*

Thomas M. Randolph

*NASA Jet Propulsion Laboratory, 4800 Oak Grove Drive, Pasadena, California 91109*

(Received 27 November 2006; accepted 19 January 2007; published online 2 March 2007)

Spectroscopic measurements of ion/neutral density ratio profiles are made inside the high-current, low-pressure discharge of a coaxial magnetoplasmadynamic thruster and show the existence of a thin ionization front, upstream in the discharge, that effectively ionizes the incoming gas to ionization levels above 50%. The measurements allow an estimate of the width of this ionization front to be on the order of a few millimeters. Due to the known existence of microturbulence in the plasma, which can produce suprathermal electrons, an explanation of the measurements based on the existence of a suprathermal tail in the electron energy distribution function is sought. A theoretical model for the width of the ionization front is combined with a multilevel excitation model for argon and shows that a Maxwellian electron distribution function cannot account for the small length scale of the ionization front, and that the latter is more consistent with an electron distribution function having a suprathermal population, the magnitude of which is estimated by comparing the model to the experiments. © 2007 American Institute of Physics.

[DOI: [10.1063/1.2646365](https://doi.org/10.1063/1.2646365)]

## I. INTRODUCTION

In a Brief Communication<sup>1</sup> Abramov and co-workers described experimental measurements that indicate that an anomalously thin ionization front may exist immediately downstream of the gas inlet of a quasistationary high-current discharge between coaxial electrodes. Unfortunately little quantitative information on this ionization front was given and its small width (axial extent) was inferred from a sharp jump in the axial intensity profiles of ion emission lines and not from a more direct measurement of the ion/neutral density ratio profile. In a concluding sentence, the authors speculated that a presence of a population of suprathermal electrons may be responsible for this abrupt ionization.

There has been a few theoretical investigations which have proposed a mechanism for the ionization of neutrals injected in such high-current low-pressure discharges. Kobayashi *et al.*<sup>2</sup> and Sheppard and Martinez-Sanchez<sup>3,4</sup> proposed that a back (upstream) diffusion of the plasma towards the gas inlet can occur, and may enhance the ionization rates leading to a shortening of the ionization region's length scale. Their models relied on a 1D description of the flow, including nonequilibrium ionization effects, under the assumption of subsonic neutral gas injection. In many real plasma sources, however, including the one used in our study, the gas is injected supersonically and the role of back diffusion may not be easily invoked. Burton and Tiliakos<sup>5</sup> considered the case of supersonic injection and their calculations suggested a role for photoionization in the initial ionization process. Their focus however was on the predischARGE gas injection region (in which they found the ionization fraction to reach a value not higher than  $10^{-4}$ ) and not on the ionization front, located within the discharge, that can lead to

almost full ionization of the incoming gas (as our measurements in Sec. III C will show). The relevance of the mechanisms proposed in these studies and their connection to our work is discussed in more detail in Sec. VI.

The above mentioned studies were conducted in the context of the magnetoplasmadynamic thruster<sup>6-8</sup> (MPDT), which is a coaxial plasma accelerator in which a high-current diffuse arc discharge ionizes and electromagnetically accelerates<sup>9</sup> the injected propellant to exhaust velocities on the order of  $10^4$  m/s (significantly exceeding those of chemical thrusters) for spacecraft propulsion applications ranging from near-earth missions<sup>10</sup> to planetary exploration.<sup>11</sup> The ionization process in the MPDT is of paramount importance to its operation (since a strongly ionized plasma must be created) and its efficiency (since the electrical power required to ionize the propellant is typically of the same order of magnitude as the directed kinetic power in the accelerated exhaust beam<sup>9</sup>). Moreover, it has been shown experimentally<sup>12</sup> that in such plasma accelerators, less than 10% of the ionization energy is recovered through recombination, even several exit diameters downstream of the acceleration region. Addressing the fundamental issues related to the existence, extent, and nature of the ionization front that controls plasma production in such high-current discharges may help improve the understanding and control of one of the most important energetic sinks in current-driven plasma thrusters and may enhance the realism of the inlet ionization models adopted in codes<sup>13-15</sup> used for the numerical simulation of such plasma devices.

We report the results of a study in which, first, we experimentally ascertain the existence of a thin ionization front through which the neutral gas flow, injected in a high-current (100–480 A) low-pressure ( $10^2$  mTorr) discharge, is almost fully ionized. We describe the ionization front and its axial

<sup>a)</sup>This paper is dedicated to the memory of Woldemar von Jaskowsky.

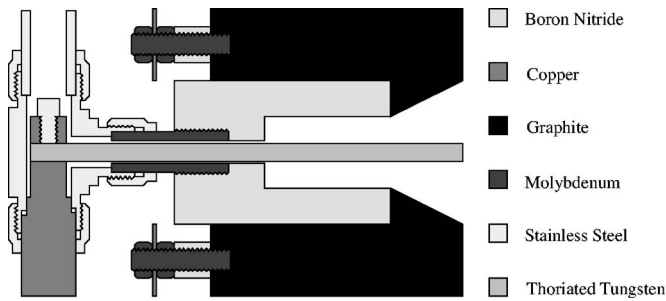


FIG. 1. Schematic drawing of standard coaxial MPD thruster.

extent quantitatively using emission spectroscopy in the diffuse high-current discharge inside the interelectrode region of a coaxial steady-state magnetoplasmadynamic thruster. Since current-driven microinstabilities and their effects have been experimentally observed<sup>16–18</sup> in the plasmas of such devices (and in particular<sup>16</sup> the same device used in our study) and the resulting microturbulence is known to cause significant suprathermal electron heating and anomalous transport,<sup>18,19</sup> we look into the role of suprathermal electrons which has not been considered in previous studies of the ionization process in such devices. Specifically, we quantify the extent to which a Maxwellian electron energy distribution function fails to explain the measured width (axial extent) of the ionization front, and calculate the magnitude of the suprathermal electron tail needed to account for the experimental measurements.

We start in Sec. II with a description of the facilities, hardware and optical diagnostics used to obtain the results discussed in Sec. III. The measured ion/neutral density profiles, which allow estimating the ionization front's axial extent, are presented and discussed in Sec. III C. A theoretical model for the front's width based on a multilevel atomic model of argon, and an electron energy distribution function that allows for a suprathermal tail is developed in Sec. IV and used to explain the measurements. The results are summarized in the final section.

## II. EXPERIMENTAL SETUP

### A. Hardware and facilities

A schematic drawing of the longitudinal cross section of the standard-configuration 20-kW-class self-field MPD thruster is shown in Fig. 1. The coaxial device, also used and described in previous studies,<sup>16</sup> consists of a cylindrical graphite anode (outer electrode) with an exit diameter of 3.5 cm and a tungsten cathode rod (central electrode) with a diameter of 0.64 cm. The cathode is connected to the power supply by a copper bus bar and the anode is connected to ground through a 300 W resistor. A boron nitride insert between the two electrodes serves as an insulator. Propellant is injected annularly between the cathode/insulator interface. Small circumferential triangular grooves on the anode/body assist radiative cooling. Water cooling is provided at the anode and cathode bus connections to the power lines. The thruster in this study was operated with an argon mass flow rate of

7 mg/s at current levels between 100 A and 480 A, which span the nominal MPDT operation regime defined by<sup>9</sup>

$$\xi \approx 1, \quad (1)$$

where  $\xi$  is the electromagnetic scaling number (a measure of how far the current is from the level corresponding to an exhaust kinetic energy equal to the ionization potential) discussed in Ref. 9 and given by

$$\xi \equiv J \left[ \frac{\dot{m}^{1/2} (2\epsilon_i/m_i)^{1/4}}{\left( \frac{\mu_o}{4\pi} \ln \frac{r_a}{r_c} \right)^{1/2}} \right]^{-1}. \quad (2)$$

Here  $J$  is the total discharge current,  $\dot{m}$  is the mass flow rate,  $r_a/r_c$  is the effective anode to cathode ratio ( $\approx 5$ ) and  $\epsilon_i$  and  $m_i$  are the ionization potential and atomic mass of the propellant. For the conditions stated above and argon propellant, we have  $0.5 \leq \xi \leq 2.5$ , and the two current levels, 100 A and 480 A, selected for this study, correspond to the lower and upper bounds of this nominal operation range.

The terminal voltage ranged between 20 and 40 V and the typical duration of steady state thruster firings is between 20 and 40 s. All data reported here were obtained during the steady-state operation mode reached within 5 s of ignition.

The thruster is placed at one end of a large vacuum facility, consisting of a 1.5 m diameter by 6.4 m long steel tank pumped by a 1.2 m diffusion pump, which is backed by a Roots blower and mechanical pump. This vacuum system maintains a background pressure below  $5 \times 10^{-4}$  Torr during thruster operation. The high-current discharge is initiated using a high-voltage (2000 V) capacitor bank which enables a 50 kW high-current power supply to drive the thruster into steady-state operation.

To obtain optical access to the thruster interelectrode region, two major modifications were made to the standard MPD thruster described above. The first one consisted of a 3 mm wide radial slot machined from the interior surface of the insulator to the exterior surface of the graphite body as shown in Fig. 2. The 7 cm long slot extends axially from the propellant inlet port to the thruster exit plane allowing optical access to the entire interelectrode region. A quartz window, secured by a ceramic holder, is used to prevent propellant flow out the slot. A fiberglass thread is used to secure the ceramic holder and provide a well defined axial geometric reference on all recorded spectra.

One concern for obtaining accurate spectroscopic data from this thruster configuration was discharge asymmetries induced by the radial slot. The thruster was checked for asymmetries in electron density and temperature profiles by an existing Langmuir probe system.<sup>16</sup> Measurements made in the near field plume revealed that no major radial asymmetries existed. Visual inspections of the interelectrode region showed that no significant preferential current attachment occurred during operation.

The second modification was the replacement of the standard cathode shown in Fig. 1 with a composite cathode shown in Fig. 3 that moves the discharge current pattern downstream enough so that the region where the injected gas encounters the discharge is visible through the optical access

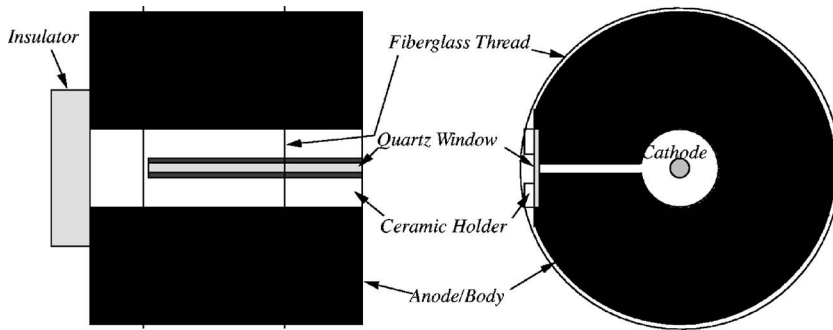


FIG. 2. Schematic drawing of the MPD thruster showing the radial slot for optical access. Left panel: side view; right panel: front view.

window described above. This composite cathode consists of a machined thoriated tungsten piece with boron nitride and copper sleeves slipped over its shaft. The copper sleeve provides an electrical connection between the copper bus and thoriated tungsten shaft, while the boron nitride sleeve restricts current attachment to the thoriated tungsten tip.

### B. Spectroscopic system

The optical system used to analyze the radiation emitted from the MPDT interelectrode region is shown in Fig. 4. Light emitted from the interelectrode region passes through the radial slot in the thruster and a quartz window in the vacuum chamber, and is collected by an achromatic lens. A first surface mirror reflects the emitted light through a dove prism, which rotates the horizontal image of the thruster slot and aligns it with the 2 cm long vertical spectrometer entrance slit. The 0.75 m Czerny-Turner spectrometer disperses the emitted radiation along its output plane, the abscissa corresponding to wavelength and the ordinate corresponding to the thruster axial position.

The optical system is focused in the interelectrode region at a radial position midway between the inner and outer radii of the discharge chamber. Spectroscopic data obtained in this fashion have fine spatial resolution (better than 0.2 mm) but since the lens focuses over an approximately 1 cm radial range, the radiation profile is essentially radially integrated over that distance. The radially integrated measurements can be taken to be representative of the average properties of the bulk interelectrode plasma since plasma properties are known to be relatively constant throughout most of this region,<sup>1,20–22</sup> unlike in the exhaust plume where they have strong gradients. Consequently we expect the assumption of radial uniformity to hold downstream only to the beginning of the expansion region, i.e.,  $x \leq 4.4$  cm in Fig. 5.

The resulting photographic spectra are digitized with an 8-bit (300 dpi) scanner and analyzed on a personal computer.

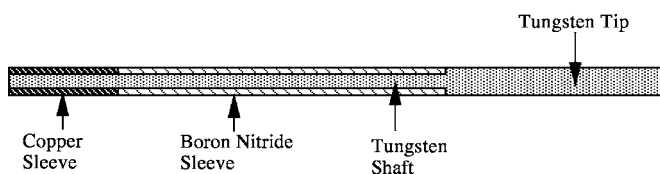


FIG. 3. Schematic drawing of the composite cathode.

Each spectrum represents a three-dimensional array of intensity, wavelength and axial position along the thruster's axis of symmetry.

### III. EXPERIMENTAL RESULTS

An extensive identification of emission lines in this plasma over a wide spectral range (3491–5740 Å) and at various current levels (100–490 A) was reported in Ref. 23. Although noticeable levels of impurity species were found to exist in the spectra due to erosion product from the insulator sleeve, they are all *upstream* of the insulator sleeve/cathode interface and do not contribute significantly to the interelectrode plasma. Through weight and volume loss considerations, the total impurity contribution to the interelectrode plasma through erosion of electrode and insulator materials was found to not exceed a few percent of the argon mass flow rate.<sup>23</sup>

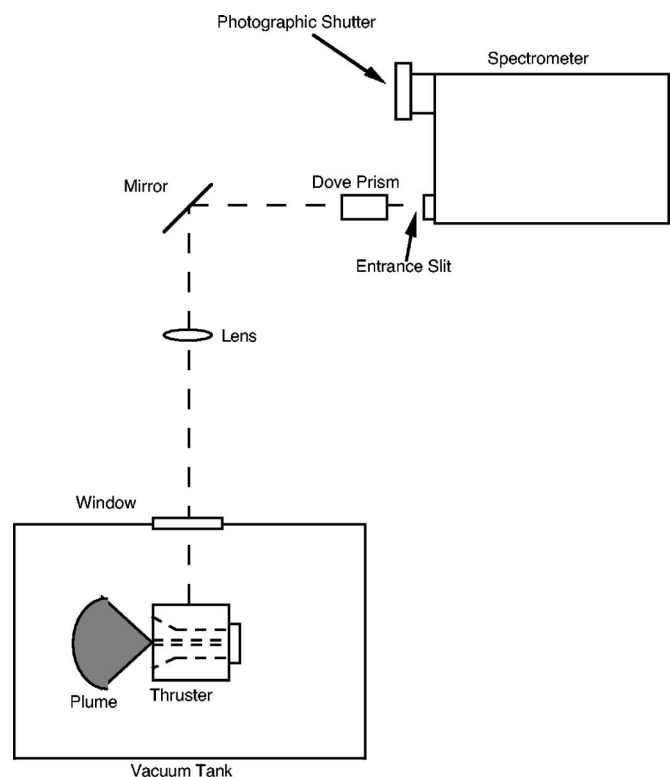


FIG. 4. Experimental setup.

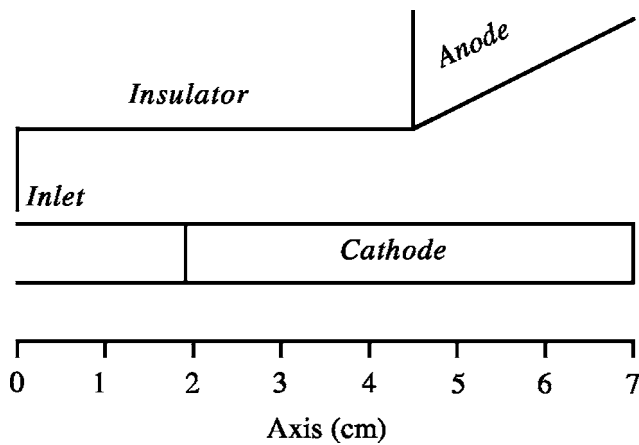


FIG. 5. Schematic of the thruster's interelectrode region showing the axial abscissa that corresponds to the  $x$  axis of all the profile plots.

### A. Argon ionic and atomic intensity profiles

The intensity profiles for the 4014 Å AII and 4259 Å AI emission lines corresponding to the geometry shown in Fig. 5 are shown in Figs. 6 and 7, respectively, for low (100 A) and high current (480 A) levels. Comparison in absolute intensity between the 100 A and 480 A profiles should not be made due to the different exposure times and spectrometer slit widths used to compensate for the difference in overall brightness.

The intensity drop at the 4.4 cm point in each line profile is due to the fiberglass thread, used to secure the quartz window to the thruster body. The dramatic intensity drop that occurs within several millimeters of the thruster exit point and the low intensity in the immediate vicinity (a few mm) of the inlet are due to the vignetting effect of the spectrometer mirrors. The use of a noncylindrical lens also contributes to optical aberrations at these points. Consequently, data within several millimeters of the inlet and exit region should not be viewed with any confidence.

We will address quantitatively the ion/neutral density ratios in Sec. III C but already some general comments on the extent of the initial ionization region can be drawn from these two figures.

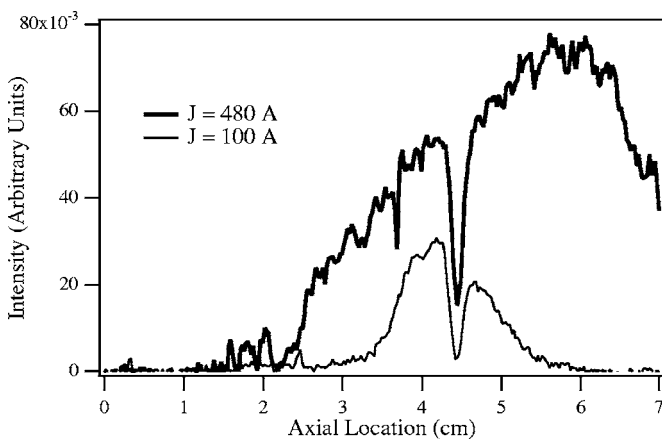


FIG. 6. AII 4014 Å line intensity versus thruster axis at two current levels. Argon mass flow = 7.0 mg/s.

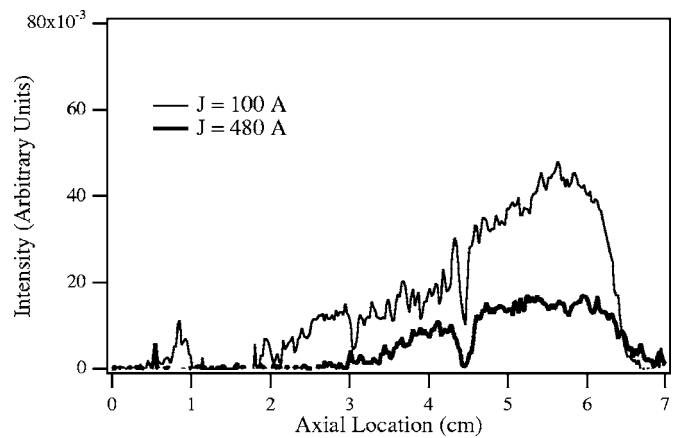


FIG. 7. AI 4259 Å line intensity profile. Same conditions as Fig. 6.

In the 100 A case, the 4014 Å AII emission line intensity rises sharply at  $x \approx 3.5$  cm, approximately 1.6 cm downstream of the current attachment point at the junction between the boron nitride sleeve and the exposed tungsten cathode. The 4259 Å AI emission line profile is comparatively flat at  $x \approx 3.5$  cm; therefore the propellant ionization must be increasing dramatically over a region that has an axial extent of about 3 mm. When the current is increased to 480 A, the 4014 Å AII emission line front moves upstream to within 0.5 cm of the current attachment point.

This type of interelectrode ionization behavior has been reported briefly and qualitatively by Abramov and co-workers in Refs. 1. Their photographic spectra revealed the existence of characteristic ionization dimensions on the order of a few millimeters or less. The shift of the characteristic ionization front upstream, as the parameter  $J^2/\dot{m}$  was increased, was also observed.

### B. Electron temperature profiles

Electron temperatures, needed for the determination of ion/neutral ratios, were obtained from the ratio of excited state emission line intensities according to the following prescription:<sup>24</sup>

$$kT_e = \frac{E_n - E_l}{\ln\left(\frac{\lambda_{lk} A_{nm} g_n I_{lk}}{\lambda_{nm} A_{lk} g_l I_{nm}}\right)}, \quad (3)$$

where  $k$  is the Boltzmann constant,  $T_e$  is the electron temperature,  $E_n$  is the energy of the excited state with respect to ground,  $\lambda_{lk}$  is the wavelength of the transition between states  $l$  and  $k$ ,  $A_{nm}$  is the transition probability from state  $m$  to  $n$ ,  $g_n$  is the degeneracy of the excited state, and  $I_{nm}$  is the intensity of the emission line. The subscripts  $n$  and  $l$  refer to the upper state of a given transition and the subscripts  $m$  and  $k$  refer to the lower state. Transition probabilities and degeneracies for AII were taken from Refs. 25–27. The implicit assumption of an optically thin plasma is well justified for nonresonant transitions in our low-pressure discharge ( $T_e \approx 1$ – $2$  eV,  $n_e \approx 10^{13}$ – $10^{14}$  cm<sup>-3</sup>). Also, the assumption of equilibrium between the excited states  $n$  and  $m$  is well justified for the range of electron densities and temperatures of this

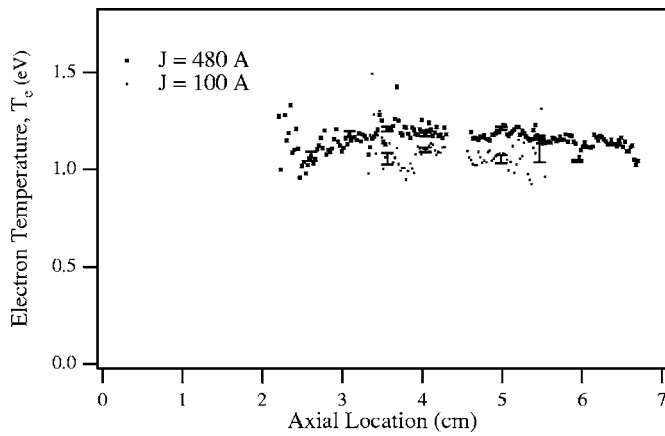


FIG. 8. Electron temperature profiles obtained from the relative line intensities of the 4014 Å and 4104 Å lines. Same conditions as Fig. 6.

discharge.<sup>24</sup> The electron temperature measurements obtained from this method were compared to those obtained from the method of a Boltzmann line fit and were found to be in good agreement.<sup>23</sup>

The two primary sources of error in such electron temperature measurements are uncertainties in the Einstein coefficients, and the resolution of the relative intensity measurements. Errors arising from the uncertainty of the Einstein coefficients grow linearly with  $T_e$ ; but such errors only affect the absolute measurement of the electron temperature. With uncertainties of 10% and 26% for the 4014 Å and 4104 Å transitions, respectively, the resulting error in electron temperature at 1 eV is 0.12 eV. Errors induced by relative intensity uncertainties are primarily the result of the scanner's bit resolution and dominate the error bars shown in Fig. 8 where the resulting electron temperature profiles for each of the two current levels are plotted.

Both profiles are relatively constant over the thruster axis, only undergoing an approximately 15% temperature rise at the upstream edge. As the current is increased from 100 A to 480 A; the electron temperature, throughout the interelectrode region increases by about 15% only. This insensitivity of the electron temperature to both the current level and the spatial location within the discharge is consistent with the results of previous measurements<sup>1,21</sup> at much higher power (megawatt) power levels.

### C. Ion/neutral ratio profiles

By comparing the relative intensities of ion and neutral emission lines, it is possible to determine the ion/neutral number density ratio. The intensities of atomic emission lines are directly proportional to the excited state number density<sup>24</sup>

$$I_{lk} \propto \frac{A_{lk} N_l}{\lambda_{lk}}, \quad (4)$$

where  $N_l$  is the number density of state  $l$ . In a nonequilibrium plasma, the excited state number density is related to the ground state number density (subscript 1 referring to the ground state) by a modified Boltzmann distribution<sup>28</sup>

$$N_l = B_l N_1 \frac{g_l}{g_1} \exp\left(\frac{-E_n}{kT_e}\right), \quad (5)$$

where  $B_l$  is the nonequilibrium coefficient for state  $l$  and accounts for the departure from equilibrium for the excited states due to radiation escaping the plasma, and  $g_n$  is the excited state degeneracy. By taking the ratio of ion and neutral emission line intensities, and substituting Eq. (4) for the ion and neutral excited state number densities, the ratio of ion/neutral ground number densities can be determined,

$$\frac{N_1^+}{N_1} = \frac{\lambda_{nm}^+ A_{lk} g_l^+ I_{nm}^+ B_l}{\lambda_{lk} A_{nm}^+ g_n^+ I_{lk} B_n^+} \exp\left(\frac{E_n^+ - E_l}{kT_e}\right), \quad (6)$$

where the superscript + refers to the ionic state. For the nonequilibrium, low temperature conditions investigated here, the total ion and neutral number densities are well approximated by the population of their respective ground states.<sup>29</sup>

Using a radiative-collisional argon plasma model, the nonequilibrium coefficients were found to be well approximated by the ratio of collisional to radiative de-excitation rates of the given excited states (Ref. 23, Appendix A),

$$B_l = \frac{N_e F_{lk}}{\sum_{k<l} A_{lk}}, \quad (7)$$

where  $N_e$  is the electron number density and  $F_{lk}$  is the electron collisional de-excitation rate, expressions for which were taken from Drawin.<sup>30</sup> By substituting Eq. (6) for ion and neutral states, Eq. (5) becomes independent of electron density; therefore ion/neutral ratio measurements can be made with a known electron temperature (from the relative intensities of two AII emission lines) by comparing the relative intensity of an AI and AII emission line.

Specifically, we compare the relative intensities of the 4014 Å AI and 4259 Å AII emission lines. The transition probability for the argon 4259 Å line was determined from Ref. 31. The energy level structure and additional needed transition probabilities were taken from Refs. 32–35. Collisional coefficients for Drawin's electron collision de-excitation rate expression for AI were obtained from Ref. 36.

Error sources in ion/neutral density ratio measurements are essentially the same as those in electron temperature measurements; however the resulting uncertainty is much larger due to the exponential dependence on electron temperature in Eq. (6). Again the effects of the scanner's bit resolution on the uncertainty in relative line intensity dominate the error bars associated with the measured ion/neutral ratio profiles shown in Fig. 9. These error bars become larger at the ion/neutral ratio profile edges where either the AI or AII emission line signal eventually drops into the noise level.

For the 100 A case, we see from Fig. 9 that the propellant ionization level increases by an order of magnitude in an approximately 3 mm front at  $x=3.5$  cm. The drop in the ion/neutral density ratio further downstream should not necessarily be taken as a measure of recombination because, as already mentioned in Sec. II B, the assumption of radial uniformity cannot be expected to hold in the expansion region ( $x \geq 4.4$  cm).

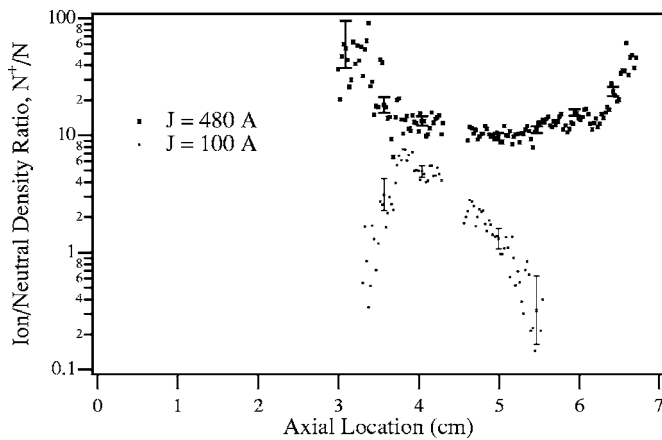


FIG. 9. Profiles of ion/neutral number density ratio at two current levels. Same conditions as Fig. 6.

As the current is increased to 480 A, the peak ionization point becomes higher and moves upstream; however the ionization front's width (axial extent) cannot be accurately measured, unlike the 100 A case, due to a weak AI signal in this region. For the same reason stated in the previous paragraph, the rise in the ion/neutral ratio for  $x \geq 4.4$  cm cannot be taken with confidence.

Although the ionization front's width cannot be accurately measured for the 480 A case, it cannot be longer than 1 cm; because the current attachment point ( $x = 1.9$  cm) is only about 1 cm upstream of the peak ionization point ( $x \approx 3$  cm). This provides an upper bound for the ionization front dimension but it is likely, given the higher energy density that must be available at the higher current and the observed upstream recession of the ionization region, that the actual ionization front's width for the 480 A case is even smaller than that (3 mm) measured more accurately at 100 A.

From both profiles we can also deduce that the ionization fraction defined as  $N^+/N^++N$  reaches values as high as 90% and above. Within the experimental uncertainty expressed by the error bars on this plot, we can conservatively state that the ionization fraction immediately downstream of the ionization front is at least 50% for the nominal operation regime investigated here ( $0.5 \leq \xi \leq 2.5$ ).

#### IV. THEORETICAL INVESTIGATION

From the above experimental investigation we learn that the width of the ionization front,  $\Delta x_i$ , for the parameters of our plasma, is typically on the order of a few millimeters and does not exceed 1 cm. The question we will now address is whether this small length scale can be explained by a Maxwellian electron distribution function (EEDF) with an average electron temperature equal to that measured and reported in Sec. III B. We will find out that such a Maxwellian EEDF falls considerably short of explaining the measured ionization front length scale, which is much smaller than the theoretically predicted one even under the most favorable conditions for the ionization kinetics. The smallness of this length scale, and the fact that strong current-driven microinstabilities are known experimentally to exist in this plasma<sup>16,17</sup> and

are of the type that produces suprathermal electrons,<sup>19</sup> lead us to consider the role of an EEDF with a suprathermal tail in enhancing the ionization process. Consequently we will carry out an analytical estimate of the ionization front's width using a detailed atomic physics model for argon and an EEDF that allows for the existence of such a tail. By setting the tail parameter to zero, we recover the Maxwellian EEDF which will allow us to contrast the "classical" prediction for  $\Delta x_i$  with the above measured range. Furthermore, by allowing the tail parameters to adjust to match the measured data we obtain a measure of the magnitude of the electron suprathermal tail required to explain the experiments.

#### V. A MODEL FOR A MINIMUM IONIZATION FRONT WIDTH

Consider a 1D ionization region of extent  $\Delta x_i$  in which neutral gas enters at position  $x_0$  and reaches maximum ionization at position  $x_0 + \Delta x_i$ . Let  $T_e$  and  $n_e$  be the average values of the electron temperature and density in that region. Making the good assumption that the ionization is due to electron impact with the incoming neutrals we can write the following continuity equation:

$$\nabla \cdot (n_n v_n) = R_{en}^{(i)}, \quad (8)$$

where  $n_n$  and  $v_n$  are the density and velocity of the neutrals, respectively, and  $R_{en}^{(i)}$  represents the reaction rate of the ionization process.

In terms of the *rate coefficient*  $K_{en}^{(i)}$ , defined as

$$K_{en}^{(i)} \equiv R_{en}^{(i)} / n_e n_n, \quad (9)$$

the above equation, in 1D, becomes

$$\frac{d}{dx} (n_n v_n) = n_e n_n K_{en}^{(i)}. \quad (10)$$

By approximating the spatial derivative using finite changes over the region's extent  $\Delta x_i$  (assuming that this distance is appropriately small) we have

$$\frac{n_n \Delta v_n + v_n \Delta n_n}{\Delta x_i} \approx n_e n_n K_{en}^{(i)}, \quad (11)$$

which can be solved for  $\Delta x_i$ ,

$$\Delta x_i \approx \frac{\Delta n_n}{n_n} \frac{v_n}{n_e K_{en}^{(i)}}, \quad (12)$$

where we have assumed that the neutrals are not accelerated much in this region (i.e.,  $\Delta v_n \approx 0$ ), which is a good assumption at the upstream end of the acceleration region.

Since we expect the measured  $\Delta x_i$  to be significantly shorter than the value calculated with a Maxwellian EEDF, we seek a model and an estimate of the *minimum* possible  $\Delta x_i$ . If this minimum possible  $\Delta x_i$  calculated with a Maxwellian EEDF is larger than the experimentally measured value, we will calculate the departures from the Maxwellian EEDF (in the form of a suprathermal tail) needed to explain the experimental data.

In order to minimize  $\Delta x_i$  we neglect all reactions that tend to increase  $\Delta x_i$  and thus limit ourselves to collisional excitation and neglect the reverse processes. This also carries

the implicit assumption that once an atom is in a highly excited state it is easily (and is thus considered) ionized. Radiative absorption is one mechanism that could theoretically enhance ionization and thus shorten  $\Delta x_i$  but it will not be considered here as it is negligible at the low temperature ( $T_e \approx 1-2$  eV) and low density ( $n_e \approx 10^{13}-10^{14}$  cm $^{-3}$ ) conditions of such optically thin plasmas.

Consistent with the above assumptions, we consider, instead of the ionization process represented by the subscript ( $i$ ) in the above expressions, excitation processes that can bring the atom from the ground level (denoted by 1) to an excited level  $j$  from which it can be easily ionized. We therefore write

$$\Delta x_i \approx \frac{\Delta n_n}{n_n} \frac{v_n}{n_e \sum_{j>1} K_{en}^{1 \rightarrow j}}. \quad (13)$$

Furthermore, since we expect considerable ionization to occur in the ionization region, we take  $\Delta n_n/n_n$  to be of order unity and write the final expression

$$\Delta x_i \approx \frac{v_n}{n_e \sum_{j>1} K_{1j}}, \quad (14)$$

where we have replaced the particle subscripts  $e$  and  $n$  with the energy level transition notation  $1j$ , which represents transition from the ground level to the excited level  $j$ .

In order to estimate  $\Delta x_i$  using the above expression we need to evaluate the integrals associated with the reaction coefficients for the relevant collisional excitation reactions<sup>29</sup>

$$K_{ij} = \left(\frac{2}{m_e}\right)^{1/2} \int_{\epsilon_{ij}}^{\infty} F(\epsilon) Q_{ij}(\epsilon) \epsilon^{1/2} d\epsilon \quad (15)$$

where as expected for a threshold-type collisional reaction, the lower limit of the integral has been set to the threshold energy for that transition  $\epsilon_{ij}$ , below which the corresponding cross section  $Q_{ij}$  vanishes.

The evaluation therefore requires

- a model of the EEDF,  $F(\epsilon)$ ,
- expressions for the relevant cross sections,  $Q_{ij}$ ,
- an atomic model of the gas in question.

We start in Sec. V A, with a model for the electron energy distribution function that allows the representation of suprathermal electron tails such as those produced by the nonlinear effects of plasma microturbulence. In Sec. V B, we describe aspects of the calculations of collisional excitation reaction rates that are central to our investigation. The resulting numerical model is then used in Sec. V C for a study of the parametric dependencies of the minimum ionization characteristic length on the tail parameters. The calculations are compared with the experimental measurements reported in Sec. III C.

## A. Electron distribution function with a suprathermal tail

We start by assuming that the bulk of the electrons, corresponding to a fraction  $(1-\mu)$  of the entire distribution (where  $\mu$  is the tail fraction), are represented by a Maxwellian speed distribution with a temperature  $T_B$ ,

$$\left(\frac{dN}{N}\right)_B = \frac{4v^2}{\pi^{1/2}(2kT_B/m)^{3/2}} \exp[-mv^2/2kT_B] dv, \quad (16)$$

where the  $B$  subscripts refer to the ‘‘bulk’’ part of the distribution.

In order to control the extent and shape of the tail, we introduce a distribution for the fraction  $\mu$  representing the suprathermal tail contribution, with a velocity drift  $u_d$  and its own equivalent ‘‘temperature’’  $T_T$  which we will refer to as the ‘‘tail energy scaling parameter,’’

$$\left(\frac{dN}{N}\right)_T = \frac{4v^2}{\pi^{1/2}(2kT_T/m)^{3/2}} \frac{\exp[-m(v-u_d)^2/2kT_T]}{\Omega} dv, \quad (17)$$

where the  $T$  subscripts refer to the suprathermal part of the distribution, and  $\Omega$  is a normalization term.

The composite distribution function  $F(v)$  is the sum of the bulk Maxwellian and the tail model adjusted by their respective fractions,

$$\frac{dN}{N} = F(v)dv = (1-\mu)\left(\frac{dN}{N}\right)_B + \mu\left(\frac{dN}{N}\right)_T. \quad (18)$$

By imposing the normalization

$$\int_0^{\infty} \left(\frac{dN}{N}\right) = \int_0^{\infty} F(v)dv = 1, \quad (19)$$

we can solve for the normalization factor  $\Omega$ ,

$$\begin{aligned} \Omega &= \int_0^{\infty} \frac{4v^2}{\pi^{1/2}\left(\frac{2kT_T}{m}\right)^{3/2}} \exp\left[-\frac{m(v-u_d)^2}{2kT_T}\right] dv \\ &= 2 + \left(2\frac{u_d}{v_{thT}}\right)^2, \end{aligned} \quad (20)$$

where  $v_{thT} = (2kT_T/m)^{1/2}$  is the corresponding thermal velocity.

A parametric plot showing the shape of the resulting distribution and its tail is shown in Fig. 10, where a bulk 2 eV temperature ( $8.4 \times 10^5$  m/s) was chosen along with a tail energy scaling parameter of 6.4 eV (as discussed in Sec. VI). The drift speed was set equal to the thermal velocity at that ‘‘temperature,’’ i.e.,  $15 \times 10^5$  m/s and the tail fraction was varied parametrically.

The integral of  $F(v)dv$  is plotted as a function of  $v$  in Fig. 11 showing the contribution to the integral of a given velocity range with the varying tail fraction,  $\mu$ .

Since our goal is the calculation of reaction rates which are obtained by weighing the cross sections with  $vF(v)$  and



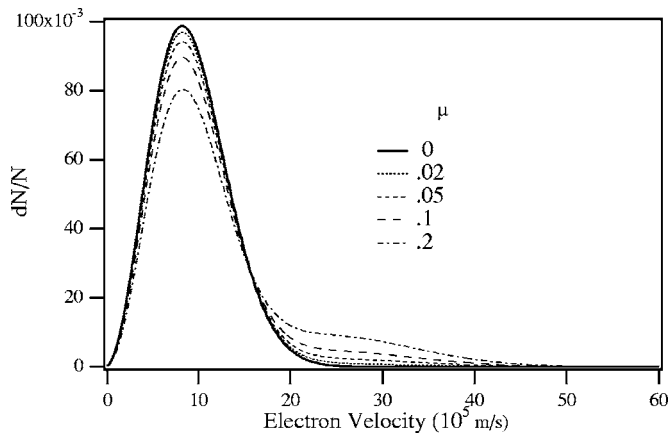


FIG. 10. Adopted distribution model for a range of tail fractions,  $\mu$ .  $T_e = 6.4$ ,  $u_d = v_{thT} = 15 \times 10^5$  m/s.

integrating from a certain reaction energy level to infinity, we choose to use the following convenient parameters:

$$u_{ij} \equiv \frac{\epsilon_{ij}}{kT}; \quad U_{ij} \equiv \frac{\epsilon}{\epsilon_{ij}}, \quad (21)$$

where the energy  $\epsilon$  becomes the implicit variable and  $\epsilon_{ij}$  represents the energy involved in going from level  $i$  to level  $j$ . The resulting model for the distribution function becomes

$$F(U_{ij})dU_{ij} = (1 - \mu) \frac{2}{\pi^{1/2}} u_{ij}^{3/2} U_{ij}^{1/2} \times \exp[-u_{ij}U_{ij}]dU_{ij} \\ + \mu \frac{e^{-\tau^2}}{\pi^{1/2}(1 + 2\tau^2)} u_{ij}^{3/2} U_{ij}^{1/2} \exp[-u_{ij}U_{ij} \\ + 2\pi u_{ij}^{1/2} U_{ij}^{1/2}]dU_{ij}, \quad (22)$$

where we have also introduced the tail spread parameter  $\tau$  defined by

$$\tau \equiv \frac{u_d}{v_{thT}}. \quad (23)$$

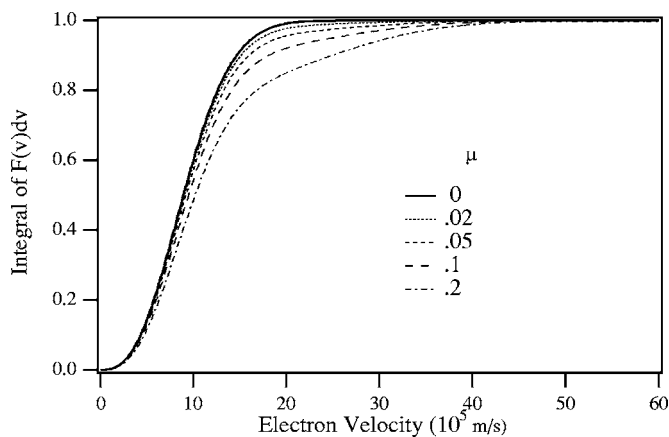


FIG. 11. Integral of the adopted distribution model for various tail fractions  $\mu$ . Same conditions as in Fig. 10.

## B. Reaction rate models for collisional excitation

In order to estimate the impact of distributions with suprathermal tails on shortening the effective ionization length from its classical values, we need to use the above model along with the relevant cross sections to calculate the associated reaction rates.

We first recast Eq. (15) to give an expression for the reaction coefficients  $K_{ij}$  in terms of the new and more convenient variable and parameters  $U_{ij}$ ,  $u_{ij}$  and  $v_{th}$  defined above,

$$K_{ij} = \langle Q_{ij}v \rangle = \int_1^\infty v_{th} u_{ij}^{1/2} U_{ij}^{1/2} Q_{ij}(U_{ij}) F(U_{ij}) dU_{ij}, \quad (24)$$

where  $Q_{ij}$  is the cross section for the transition in question. Since we are dealing with excitation by electron impact from the ground state, we have  $i=1$ .

For cross sections of atomic excitation by electron impact, we use the well-established semiempirical formulas of Drawin:<sup>30</sup>

a. For allowed transitions the cross section  $Q_{ij}^A$  is:

$$Q_{ij}^A = 4\pi a_0^2 \left( \frac{\epsilon_1^H}{\epsilon_{ij}} \right)^2 f_{ij}^A \alpha_{ij}^A \left[ \frac{U_{ij}-1}{U_{ij}^2} \right] \ln(1.25\beta_{ij}U_{ij}). \quad (25)$$

b. For parity-forbidden transitions the cross section  $Q_{ij}^P$  is:

$$Q_{ij}^P = 4\pi a_0^2 \alpha_{ij}^P \left[ \frac{U_{ij}-1}{U_{ij}^2} \right]. \quad (26)$$

c. For spin-forbidden transitions the cross section  $Q_{ij}^S$  is:

$$Q_{ij}^S = 4\pi a_0^2 \alpha_{ij}^S \left[ \frac{U_{ij}^2-1}{U_{ij}^5} \right]. \quad (27)$$

In the above,  $f_{ij}^A$  is the absorption oscillator strength for optically allowed transitions,  $\alpha_{ij}$  and  $\beta_{ij}$  are fit coefficients. All these parameters are part of the atomic physics model adopted for the calculations. Finally,  $\epsilon_1^H$  is the ionization potential of hydrogen from ground state (13.6 eV).

We consider 23 known excitation transitions from the ground level of the argon atom. These levels are part of the 65-level lumped atomic model for argon compiled and described by Vlček in Ref. 36. All the information needed to represent these 23 transitions in the above equations are listed in Table I extracted from Ref. 36.

## C. Results

We now illustrate the calculations by comparing the minimum  $\Delta x_i$  calculated from Eq. (14) with the experimentally measured values.

In order to find the shortest possible  $\Delta x_i$  from Eq. (14) we set  $v_n$  to its lowest value in the MPDT  $v_n = v_{inlet} \approx 320$  m/s and set  $n_e$  to the highest measured density<sup>16</sup>  $n_e \approx 10^{14}$  cm<sup>-3</sup>. In the same spirit we choose for the electron (bulk) temperature  $T_B$  the high end of the values measured for this thruster. Since we know that  $T_e$  does not exceed 2 eV we take  $T_B = 2$  eV. This will give the Maxwellian EEDF the best possible chance for accounting for the smallness of  $\Delta x_i$ .

TABLE I. Data for the 23 transitions considered in our calculations. A, optically allowed; P, parity-forbidden; S, spin-forbidden transitions. From Ref. 36.

Level $n$	Designation	Excitation energy (eV)	Type of transition	Coefficients $\alpha_{ij}^F$ or $\alpha_{ij}^{A,P,S}, \beta_{ij}$
1	$3p^6$	0	...	...
2	$4s[3/2]_2$	11.548	S	$6.70 \times 10^{-2}$
3	$4s[3/2]_1$	11.624	A	$1.92 \times 10^{-2}, 4$
4	$4s'[1/2]_0$	11.723	S	$9.50 \times 10^{-3}$
5	$4s'[1/2]_1$	11.828	A	$4.62 \times 10^{-2}, 4$
6	$4P[1/2]_1$	12.907	P	$3.5 \times 10^{-2}$
7	$4P[3/2]_{1,2}, [5/2]_{2,3}$	13.116	P	$1.15 \times 10^{-1}$
8	$4P'[3/2]_{1,2}$	13.295	P	$3.50 \times 10^{-2}$
9	$4P'[1/2]_1$	13.328	P	$7.00 \times 10^{-3}$
10	$4P[1/2]_0$	13.273	P	$7.00 \times 10^{-3}$
11	$4P'[1/2]_0$	13.480	P	$3.50 \times 10^{-2}$
12	$3d[1/2]_{0,1}, [3/2]_2$	13.884	S	$1.50 \times 10^{-1}$
13	$3d[7/2]_{3,4}$	13.994	S	$9.00 \times 10^{-2}$
14	$3d'[3/2]_2, [5/2]_{2,3}$	14.229	P	$4.20 \times 10^{-2}$
15	$5s'$	14.252	A	$3.71 \times 10^{-3}, 4$
16	$3d[3/2]_1, [5/2]_{2,3} + 5s$	14.090	A	$3.33 \times 10^{-2}, 4$
17	$3d'[3/2]_1$	14.304	A	$1.79 \times 10^{-2}, 2$
18	$5p$	14.509	P	$7.00 \times 10^{-2}$
19	$5p'$	14.690	P	$5.00 \times 10^{-2}$
20	$4d+6s$	14.792	A	$5.15 \times 10^{-2}, 1$
21	$4d'+6s'$	14.976	A	$3.06 \times 10^{-2}, 1$
26	$5d'+7s'$	15.324	A	$6.50 \times 10^{-4}, 1$
27	$5d+7s$	15.153	A	$3.69 \times 10^{-2}, 1$
33	$6d+8s$	15.347	A	$2.40 \times 10^{-2}, 1$

In our parametric study, we set the tail spread parameter  $\tau$  to unity (i.e.,  $u_d = v_{th,p}$ ) to reduce the number of tail control parameters, and vary the other two tail quantities: the tail fraction,  $\mu$  and the tail energy scaling parameter  $T_T$ . The integral in Eq. (24) is evaluated with a 16-point Gauss-Legendre quadrature to insure high accuracy.

Figure 12 shows results from these calculations along with the upper and lower bounds for the experimentally measured values. The Maxwellian limit is obtained when the tail

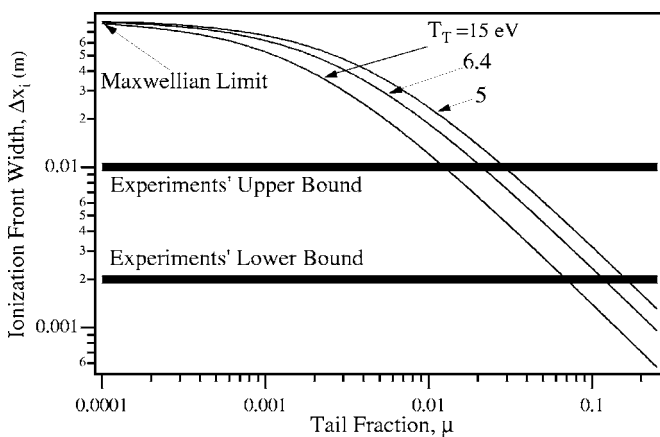


FIG. 12. Calculated minimum values of  $\Delta x_i$  as a function of the tail fraction.  $T_e = 2.0$  eV,  $\tau = 1$ .

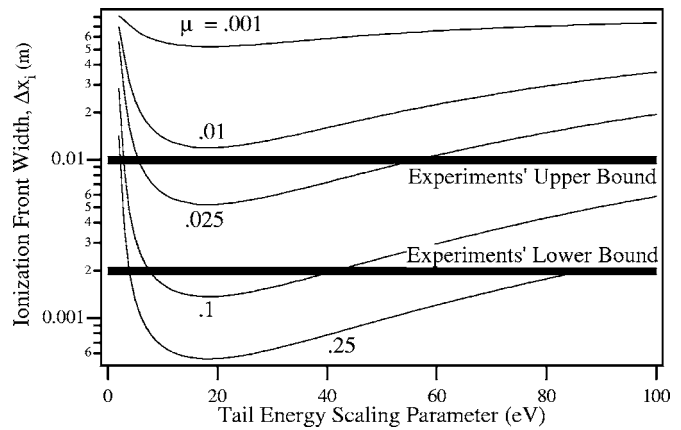


FIG. 13. Calculated minimum values of  $\Delta x_i$  as a function of the tail energy scaling parameter,  $T_T$ .  $T_e = 2.0$  eV,  $\tau = 1$ .

fraction goes to zero. It is thus clear that even under the most favorable conditions, Maxwellian electrons cannot account for the smallness of  $\Delta x_i$ . It is also clear that at these conditions, tail fractions of the order of a few percent can bring down  $\Delta x_i$  in the millimeter range that encompasses the experimentally measured values. Since we have assumed the most favorable conditions for the smallest  $\Delta x_i$ , these tail parameters represent a lower bound for the values needed to account for the experimental results.

It should also be noted that  $\Delta x_i$  is not always a monotonic function of the tail parameters due to the complex interplay between the tail's shape and the cross-section-energy dependence. Depending on the energy level and the tail parameters, contributions to  $\Delta x_i$  from allowed, spin-forbidden, and parity-forbidden transitions, alternate in importance.

An illustration of how increasing the tail's energy scaling parameter  $T_T$  can either increase or decrease  $\Delta x_i$  is shown in Fig. 13. The curves go through a minimum around 20 eV. At that minimum, tail fractions of 1% and higher can bring  $\Delta x_i$  down to within the experimental bounds.

## VI. DISCUSSION AND CONNECTION TO PREVIOUS WORK

Previous theoretical studies<sup>2-5</sup> of inlet ionization in MPD thrusters have considered three mechanisms that can potentially contribute to controlling the width of the ionization region: (1) upstream flux (from the plasma to the ionization region) of charged particles, (2) photoionization, and (3) (thermal) electron impact.

Sheppard and Martinez-Sanchez<sup>3,4</sup> treated the particular case of subsonic neutral gas injection into the MPD discharge chamber and showed that the thickness of the ionization region near the inlet is controlled by an upstream flux (back-diffusion) of electron-ion pairs. It is doubtful that the case they considered corresponds to our measurements since the low pressure in the discharge chamber of our thruster should insure that the gas flow from the choked injection annulus is supersonic by the time it reaches the ionization front, which, in our experiments, is more than 2 cm from the inlet. A supersonic gas injection, in the words of the authors, "erases any possible effect that back-diffusion may have on

inlet ionization.” Furthermore, their model, when evaluated using the relevant dimensional parameters of our experiment (mass flow rate=7 mg/s; current=100–480 A; magnetic field strength=1–4.8×10<sup>-3</sup> T;  $T_e$ =1–2 eV; channel radius =2 cm) predicts an ionization front thickness of a few centimeters at least.

Burton and Tiliakos<sup>5</sup> treat the complimentary case of subsonic inlet gas injection, which is more relevant to our experiments, and consider the roles of photoionization and electron impact in controlling the inlet ionization process. They find that while photoionization plays an initial role in inlet ionization by raising the ionization fraction from an initial level of 10<sup>-7</sup> to 10<sup>-5</sup>, it is quickly surpassed by electron impact when the ionization fraction reaches the latter level. Both mechanisms are shown to bring the ionization level to no more than 10<sup>-4</sup> over a distance of 3–6 mm. Therefore, this region of relatively very low ionization cannot be identified as the ionization front observed in our experiments and those of Abramov *et al.*,<sup>1</sup> but rather, using the term proposed by Burton and Tiliakos, as a “preionization region.” Such a region may play an important role in the ignition of the discharge, as explained by the authors, but is not the strong ionization front that is the focus of our study.

The inability of (thermal) electron impact ionization, as considered in Burton and Tiliakos’s model, to raise the ionization level beyond relatively miniscule levels over a distance of a few millimeters is not surprising in light of our results where ionization with a Maxwellian distribution (representing such a thermal electron impact process) requires a distance of many centimeters at the least to lead to substantial ionization (see Fig. 12 for the limiting case of no suprathermal tail).

Finally, it is relevant to mention the recent 2004 study of Borghi *et al.*,<sup>38</sup> where spectroscopic measurements of electron energies in the argon plasma of a MPD thruster show the existence of a suprathermal electron population. This seems to be the first time such direct experimental evidence is reported. While the measurements show a thermal electron population with a bulk temperature of 1.2 eV and a suprathermal one at more than twice that temperature (2.5 eV), the reported measurements are not in a form of an energy-resolved distribution function and thus do not allow the extraction of a value for the tail fraction.

The discussion above, along with the results of our study, compel us to deduce that a non-Maxwellian electron distribution function with a suprathermal tail is the most likely explanation for the thinness of the observed ionization front. While there could potentially be more than one mechanism in MPD thruster plasmas that could result in the generation of such a suprathermal tail, a likely suspect are the current-driven microinstabilities that have been observed experimentally and studied theoretically in the literature.<sup>16–19,37</sup> Numerical simulations of ionization driven by counterstreaming instabilities, such as those reported in Ref. 39, show that such microinstabilities can generate significant suprathermal tails. A scaling of the calculated distribution functions from such a simulation to the parameters of the MPD thruster was made in Ref. 40 and gave an estimate of 6.4 eV for  $T_T$ . (Consequently, we included a calculated curve for

that value of  $T_T$  in Fig. 12.) Since the focus of the present study is the thickness of the ionization front and not the mechanism generating the suprathermal tail, we will refrain from speculating further on their origin.

## VII. CONCLUSIONS

The above spectroscopic and theoretical analysis of the spatial extent of the plasma production region in the high-current discharge of a nominally operated MPD thruster allows us to draw the following conclusions:

1. Spectroscopic measurements of ion/neutral density ratio profiles showed that an ionization front exists upstream in the discharge and effectively ionizes the incoming gas to ionization levels above 50%.
2. The width (axial extent) of this ionization front was determined experimentally to be on the order of a few millimeters.
3. An analytical model of the ionization front’s width was developed to explain the measurements using a multi-level atomic model of argon coupled to a prescription for the electron energy distribution function that allows the representation of suprathermal electron tails such as those produced by the nonlinear effects of plasma microturbulence.
4. With the tail parameters set to zero, the resulting Maxwellian EEDF, even under the most favorable conditions, overpredicts the ionization front’s width by more than a factor of 10.
5. The measured width of the ionization front is shown to be more consistent with electron distributions having suprathermal tails as would be expected in such a plasma where current-driven microinstabilities have been experimentally observed<sup>16,17</sup> and are known to result significant suprathermal electron heating and anomalous transport.<sup>18,19</sup>
6. Tail fractions as small as a few percent were found to reduce the spatial extent of the ionization front down to the observed millimeter level.

## ACKNOWLEDGMENTS

This work was supported by research grants from NASA and the U.S. Air Force Office of Scientific Research.

<sup>1</sup>V. A. Abramov, A. K. Vinogradova, Y. P. Dontsov, Y. A. Zavenyagin, P. E. Kovrov, V. I. Kogan, and A. I. Morozov, in *Proceedings of the 8th International Conference on Phenomena in Ionized Gases* (International Atomic Energy Agency, Vienna, 1968), panel 33.1.11, p. 160.

<sup>2</sup>O. Kobayashi, K. Komurasaki, and T. Fujiwara, *Trans. Jpn. Soc. Aeronaut. Space Sci.* **38**, 126 (1995).

<sup>3</sup>E. J. Sheppard and M. Martinez-Sanchez, *23<sup>rd</sup> International Electric Propulsion Conference* (The Electric Rocket Propulsion Society, Worthington, 1993), IEPC-93-071.

<sup>4</sup>E. J. Sheppard and M. Martinez-Sanchez, *Ionization Ignition in Atomic Self-Field MPD Thruster Flows* (American Institute of Aeronautics and Astronautics, Washington, D.C., 1994), AIAA 94-3342.

<sup>5</sup>R. L. Burton and N. Tiliakos, *J. Propul. Power* **9**, 764 (1993).

<sup>6</sup>A. C. Ducati, G. M. Giannini, and E. Muehlberger, *AIAA J.* **2**, 1452 (1964).

<sup>7</sup>A. C. Malliaris, *J. Appl. Phys.* **38**, 3611 (1967).

<sup>8</sup>R. G. Jahn, *Physics of Electric Propulsion* (McGraw-Hill, New York, 1968).

- <sup>9</sup>E. Y. Choueiri, J. Propul. Power **14**, 744 (1998).
- <sup>10</sup>E. Y. Choueiri, A. J. Kelly, and R. G. Jahn, J. Spacecr. Rockets **30**, 749 (1993).
- <sup>11</sup>R. H. Frisbee and N. J. Hoffman, *SP-100 Nuclear Electric Propulsion for Mars* (American Institute of Aeronautics and Astronautics, Washington, D.C., 1996), AIAA 96-3173.
- <sup>12</sup>A. P. Bruckner and R. G. Jahn, AIAA J. **12**, 1198 (1974).
- <sup>13</sup>M. Auweter-Kurtz, H. L. Kurtz, H. O. Schrader, and P. C. Sleziona, J. Propul. Power **5**, 49 (1989).
- <sup>14</sup>K. Sankaran, L. Martinelli, S. C. Jardin, and E. Y. Choueiri, Int. J. Numer. Methods Eng. **53**, 1415 (2002).
- <sup>15</sup>K. Sankaran, E. Y. Choueiri, and S. C. Jardin, J. Propul. Power **21**, 129 (2005).
- <sup>16</sup>D. L. Tilley, E. Y. Choueiri, A. J. Kelly, and R. G. Jahn, J. Propul. Power **12**, 381 (1996).
- <sup>17</sup>E. Y. Choueiri, A. J. Kelly, and R. G. Jahn, *22<sup>nd</sup> International Electric Propulsion Conference* (The Electric Rocket Propulsion Society, Worthington, 1991), IEPC-91-100.
- <sup>18</sup>D. C. Black, R. M. Mayo, and R. W. Caress, Phys. Plasmas **4**, 3581 (1997).
- <sup>19</sup>E. Y. Choueiri, Phys. Plasmas **6**, 2290 (1999).
- <sup>20</sup>K. E. Clark, M. S. DiCapua, R. G. Jahn, and W. F. von Jaskowsky, *Quasi-Steady Magnetoplasma-dynamic Arc Characteristics* (American Institute of Aeronautics and Astronautics, Washington, D.C., 1970), AIAA-70-1095.
- <sup>21</sup>R. C. Oberth and R. G. Jahn, AIAA J. **10**, 86 (1972).
- <sup>22</sup>H. Tahara, H. Yasui, Y. Kagaya, and T. Yoshikawa, *Experimental and Theoretical Research on Arc Structure in a Self-Field Thruster* (American Institute of Aeronautics and Astronautics, Washington, D.C., 1987), AIAA-87-1093.
- <sup>23</sup>T. M. Randolph, Master's thesis, Princeton University, Princeton, New Jersey, 1994.
- <sup>24</sup>W. Lochte-Holtgreven, *Plasma Diagnostics* (Wiley, New York, 1968).
- <sup>25</sup>W. L. Wiese, M. W. Smith, and B. M. Miles, *Atomic Transition Probabilities* (National Bureau of Standards, Gaithersburg, 1969), Vol. II, NSRDS-NBS-22.
- <sup>26</sup>T. Ludtke and V. Helbig, J. Quant. Spectrosc. Radiat. Transf. **44**, 600 (1990).
- <sup>27</sup>R. I. Rudko and C. L. Tang, J. Appl. Phys. **38**, 4011 (1967).
- <sup>28</sup>S. Suckewer, J. Phys. B **3**, 380 (1970).
- <sup>29</sup>M. Mitchner and C. H. Kruger, *Partially Ionized Gases* (Wiley, New York, 1973).
- <sup>30</sup>H. W. Drawin, *Collision and Transport Cross Sections* (Euratom-CEA, Fontenay-aux-Roses, France, 1967), EUR-CEA-FC-383.
- <sup>31</sup>W. L. Wiese, J. W. Brault, K. Danzmann, V. Helbig, and M. Koc, Phys. Rev. A **39**, 2461 (1989).
- <sup>32</sup>A. M. Gomes, J. Phys. D **16**, 631 (1983).
- <sup>33</sup>K. Kastonis and H. W. Drawin, J. Quant. Spectrosc. Radiat. Transf. **23**, 1 (1980).
- <sup>34</sup>A. Kimura, H. Kobayashi, M. Nishida, and P. Valentin, J. Quant. Spectrosc. Radiat. Transf. **34**, 322 (1985).
- <sup>35</sup>A. R. Striganov and N. S. Sventitskii, *Tables of Spectral Lines of Neutral and Ionized Atoms* (Plenum, New York, 1968).
- <sup>36</sup>J. Vlcek, J. Phys. D **22**, 623 (1989).
- <sup>37</sup>E. Y. Choueiri, Phys. Rev. E **64**, 066413 (2001).
- <sup>38</sup>C. A. Borghi, M. R. Carraro, A. Cristofolini, R. Ghidini, *Plasma Conditions in the Argon Discharge of an MPD Thruster* (American Institute of Aeronautics and Astronautics, Washington, D.C., 2004), AIAA 2004-2360.
- <sup>39</sup>E. Y. Choueiri and H. Okuda, Phys. Plasmas **1**, 1669 (1994).
- <sup>40</sup>E. Y. Choueiri and H. Okuda, *23rd International Electric Propulsion Conference* (The Electric Rocket Propulsion Society, Worthington, 1993), IEPC-93-067.